A Macromodeling-Based Hybrid Method for the Computation of Transient Electromagnetic Fields Scattered by Nonlinearly Loaded Metal Structures

A Macromodeling Based Hybrid Method for the Computation of Transient Electromagnetic Fields Scattered by Nonlinearly Loaded Metal Structures

Torben Wendt, *Student Member, IEEE*, Cheng Yang, *Member, IEEE*, Heinz D. Brüns, Stefano Grivet-Talocia, *Fellow, IEEE*, and Christian Schuster, *Senior Member, IEEE*

***Abstract*—We present a hybrid numerical scheme to compute the transient electromagnetic fields scattered by a metallic structure loaded with lumped, nonlinear loads. The proposed scheme is based on three successive steps. First, the field coupling problem to the structure with the nonlinear loads removed is solved in the frequency-domain using a Method-of-Moments (MoM) formulation. The unloaded structure is thus characterized as a generalized multiport Thevenin equivalent, whose components are represented as time-domain operators by performing a set of rational approximations followed by closed-form Laplace transform inversion. Transient port voltages and currents in presence of nonlinear loads are then computed using a standard circuit solver. As a last step, the substitution theorem is used to solve the radiation problem again in the frequency domain using a MoM solver, the results of which are then translated into time-domain by means of rational approximations and recursive convolution operations. The proposed method enables an accurate and efficient evaluation of the transient nonlinearly scattered fields by the loaded structure, with a good potential for scalability to large-scale high-complexity nonlinear shields. Extensive validations are provided to demonstrate the accuracy of the proposed method, which is here applied to the characterization of energy-selective shielding for protection of sensitive devices from High-Intensity Radiated Fields (HIRF).**

I. Introduction

THREATS to today's sensitive electronic devices have many forms. Exposure to High Intensity Radiated Fields (HIRFs) can destroy unprotected devices. HIRFs can be caused by radio transmitters, base stations, lightning strikes, electrostatic discharge or Nuclear Electromagnetic Pulses (NEMPs). To make electronic systems more robust with respect to HIRFs shielding can be used. Shielding can be achieved by placing the vulnerable devices in a conductive enclosure. However, to allow for wireless communication with the outside world an opening in the enclosure is inevitable. This opening provides an exit and entrance path for both communication and HIRFs [1]. If poorly designed, an enclosure with aperture can focus destructive electromagnetic energy onto the sensitive devices.

A promising approach to mitigate the danger of HIRFs is the design of self-actuated structures using nonlinear elements. In [2] a nonlinear cover for apertures is presented. The cover is a diode grid and changes from transparent to reflecting if a hazardous energy level is exceeded. This novel shielding method achieves an adaptive electromagnetic protection that reflects potentially destructive fields while being almost transparent to weak communication signals. Recently, many other applications of nonlinearly loaded structures have been presented, e.g. frequency selective surfaces [3], [4], energy selective surfaces [5], waveform-dependent absorbing metasurfaces [6], [7], and power-dependent impedance surfaces [8]–[10].

Modelling of nonlinearly loaded structures has been a topic of computational electromagnetics since at least the late 1970s [11], [12]. The simulation methods can be generally classified into two classes. The first is based on real-time full-wave simulations, which calculate the voltages/currents of nonlinear loads and the scattering fields simultaneously in time domain. For example, the Finite-Difference Time-Domain Method (FDTD) [13], the Time Domain Finite-Element Method (TD-FEM) [14], the Partial Element Equivalent Circuit (PEEC) approach [15], and techniques based on Time Domain Integral Equations (TDIE) [16] belong to this category. The second category utilizes a combination of various full-wave and circuit solvers to compute the load responses at first, and then a post-processing to extract the fields, such as the transient convolution based technique [17]–[21], the Harmonic Balance (HB) [22] approach and the envelope tracking method [23].

This paper belongs to the second class of solvers and provides an alternative formulation with respect to the method originally presented in [2], [24]. In particular, the large-scale electromagnetic problem related to field coupling and radiation is decoupled from the small-scale problem related to interaction with lumped nonlinear components. The former can be formulated and solved in frequency domain; since the particular electromagnetic structure we are considering is open, we will resort to the Method of Moments (MoM) as the core field solver. Due to the presence of nonlinear elements, a transformation from frequency to time domain is mandatory. This step is here performed through behavioral macromodels, suitably identified through Vector Fitting (VF) techniques from sampled frequency-domain data obtained by the MoM solver.

The proposed hybrid method has several advantages compared to competing approaches. Although the problem decomposition between linear (frequency-domain) electromagnetic and nonlinear (time-domain) circuit subproblems is not new, here we perform the conversion between frequency and time

T. Wendt, C. Yang, H. Brüns and C. Schuster are with the Institute of Electromagnetic Theory, Hamburg University of Technology, Harburger Schloßstr. 20, 21073 Hamburg, Germany (email: torben.wendt@tuhh.de, cheng.yang@tuhh.de, schuster@tuhh.de).

S. Grivet-Talocia is with the Dept. of Electronics and Telecommunications, Politecnico di Torino, C. Duca degli Abruzzi 24, 10129 Torino, Italy (email: stefano.grivet@polito.it).

This work is supported by the German Research Foundation.

domains through high-performance macromodeling schemes, leveraging on recent developments that guarantee numerical robustness, stability and efficiency. This approach has no limitations on the nature of excitation signals, which are not required to be narrowband or periodic as in Harmonic Balance or envelope tracking methods. Moreover, the linear electromagnetic subproblem and consequent macromodels are computed only once in a preprocessing *offline* step, allowing for fast repeated (*online*) transient analyses with different loading components and excitation waveforms and/or energy levels. This is obviously not allowed with direct transient solvers that integrate lumped nonlinear loads (e.g., FDTD or FIT), which require to repeat the complete full-wave simulation anytime a component or excitation is varied. The presented approach differs from [2,24] specifically by (i) performing the transient analysis through using a legacy circuit solvers of the SPICE class and finally, (ii) computing the nonlinearly scattered electromagnetic field at various observation points through dedicated recursive convolution schemes, which prove very efficient and easily parallelizable. Finally, the adopted problem decoupling has the potential for improved scalability when increasing the number of nonlinear loads to hundreds or thousands, as may be required by the energy-selective shielding application that motivates this work. Detailed scalability studies will be addressed in a future report.

Additional advantages or proposed approach become evident when considering the specific electromagnetic scattering problem under investigation. All structures of interest are metallic and embedded in an open computational domain. For such structures, the frequency-domain Method of Moments (MoM) provides the most appropriate EM formulation, since only surface unknowns (currents on metal objects) are solved for, without any need of truncating the computational domain. Conversely, transient solvers (FDTD, FIT) need to artificially truncate the computational domain with an absorbing layer such as Perfectly Matched Layer (PML) [25]; we show in Sec. V-A that, when combined to strong nonlinearities with rectifying behavior, the PML may lead to inaccurate results due to mixing and downconversion of energy to low frequencies. In addition, transient (differential) solvers compute fields in a discrete volume mesh, requiring a much larger number of unknowns with respect to MoM. For these reasons, the MoM (integral) formulation in the frequency domain is our preferred EM solver. We do not consider time-domain integral equation solvers since the presence of nonlinear terminations may have a detrimental effect on solver stability, which is instead guaranteed by the adopted macromodeling approach which enforces both stability and passivity, see Sec. III.

This paper is structured as follows. Section II provides a high-level description of the main components of proposed hybrid approach. Section III reviews some background material on macromodeling, highlighting those aspects that are relevant for this work. Section IV provides a detailed description of all computational stages, whereas critical issues that are relevant for validation, which are related to computational domain truncation and lumped port modeling, are addressed in Sec. V. Finally, Sec. VI presents and discusses numerical results, with conclusions drawn in Sec. VI.

II. General Modelling Approach

This section provides a general description of the proposed method, with reference to Fig. 1. An electrically large, perfectly electrically conducting (PEC) structure is loaded with electrically small, nonlinear elements connected at lumped and electrically small ports, as depicted in Fig. 1a. The structure is illuminated by a plane wave pulse with electric field amplitude $\mathcal{E}_{\text{inc}}(t)$, which is scattered by the structure. Due to the nonlinear loads, the scattered field caused by induced currents on the structure depends nonlinearly on $\mathcal{E}_{\text{inc}}(t)$. The objective is to compute the total electric field $\vec{\boldsymbol{\mathcal{E}}}_{\text{obs}}(t, \vec{\boldsymbol{r}}_o)$ at a set of observation points $\vec{\boldsymbol{r}}_o$. Our approach divides this process into three steps.

A. Characterization of field coupling at lumped ports and extraction of the Thevenin equivalent of the metallic structure

Starting from the structure depicted in Fig. 1a, we detach the nonlinear loads from the ports and we characterize the resulting field-excited structure through a generalized Thevenin equivalent [26], as shown in Fig. 1d. This requires the solution of two independent field problems, which are carried out with the MoM solver [27] in the frequency domain. First, we compute the induced open circuit voltages $\boldsymbol{V}_{\text{oc}}(j\omega)$ by leaving each port open-circuited and exciting the structure with the incident field (Fig. 1b). Second, we evaluate the impedance matrix $\breve{\boldsymbol{\mathcal{Z}}}(j\omega)$ of the structure by exciting each port through a current source and evaluating the corresponding port voltages, with the incident field deactivated (Fig. 1c). Further details are discussed in Sec. IV-A.

B. Solution of transient port voltages with nonlinear loading

Considering the equivalence established in Fig. 1e, we cast the generalized Thevenin equivalent in time-domain by: i) computing a stable and passive state-space macromodel of the impedance matrix, which is then realized as a SPICE network, see Sec. III-A; ii) apply a frequency-domain rational function approximation to the open-circuit voltages $\boldsymbol{V}_{\text{oc}}(j\omega)$, so that an accuracy-controlled closed-form time-domain waveform $\boldsymbol{v}_{\text{oc}}(t)$ is achieved through inverse Laplace transform (Sec. III-B). The corresponding time-domain lumped circuit obtained by connecting the nonlinear elements to each port (Fig. 1e) is then solved in time-domain using a circuit solver. The computed transient port voltages $\boldsymbol{v}(t)$ are the same (net of all numerical approximations involved in all computations) that we would observe by solving directly the nonlinear electromagnetic field coupling problem depicted in Fig. 1a. Note that, by the Substitution Theorem [28], once we know the actual transient port voltages $\boldsymbol{v}(t)$, we can replace the nonlinear terminations with ideal voltage sources with the same values $\boldsymbol{v}(t)$ without affecting any other electrical variable of interest (see Fig 1f), including the transient currents through the structure, which are used in the next step.

C. Computation of field at observation points

Based on the above considerations, the original nonlinear scattering problem is reformulated as an equivalent linear

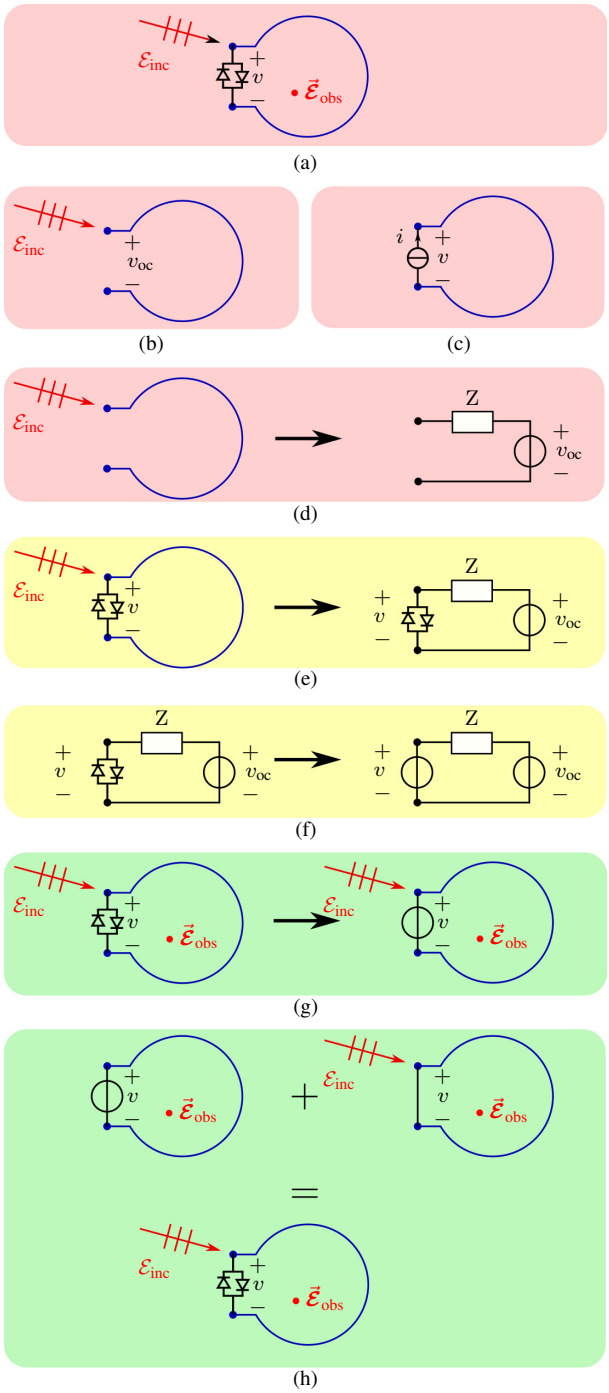

Fig. 1. Graphical description of the proposed modeling flow. (a)-(d): characterization of field coupling at lumped ports and extraction of the generalized Thevenin equivalent of the metallic structure (red, Sec. II-A); (e)-(f): Solution of transient port voltages with nonlinear loading (yellow, Sec. II-B); (g)-(h): Computation of field at observation points (green, Sec. II-C).

scattering problem, by replacing the nonlinear terminations with known lumped voltage sources $\boldsymbol{v}(t)$, see Fig. 1g. This linear scattering/radiation problem can be solved using the frequency-domain MoM solver, with a postprocessing transformation between frequency and time-domain. Due to the presence of two source terms, one related to the incident field and one to the lumped voltage sources, we apply superposition by solving the two problems independently, as depicted in Fig 1h. In particular, the radiated field is obtained as the superposition of the field scattered by the short-circuited structure (i.e. by setting $\boldsymbol{v}(t) = 0$) with the field radiated by the antenna-like structure excited by $\boldsymbol{v}(t)$ with the incident field deactivated. Details about this step are reported in Sec. IV-C.

D. Some remarks on notation

Throughout this work, normal fonts are used for scalar x and boldface fonts for vectors $\boldsymbol{x}$, matrices $\boldsymbol{X}$ and tensors. Time-domain and frequency-domain port signals are typeset in lower $\boldsymbol{v}(t)$ and upper case $\boldsymbol{V}(j\omega)$, respectively. Incident (electric) field waveform is denoted with $\mathcal{E}_{\text{inc}}(t)$ and $E_{\text{inc}}(j\omega)$ in time and frequency domain, respectively, with the corresponding vector fields at position $\vec{\boldsymbol{r}}$ denoted as $\vec{\boldsymbol{\mathcal{E}}}_{\text{inc}}(t, \vec{\boldsymbol{r}})$ and $\vec{\boldsymbol{E}}_{\text{inc}}(j\omega, \vec{\boldsymbol{r}})$.

Calligraphic fonts are used for exact (continuous) frequency-domain operators $\breve{\boldsymbol{\mathcal{C}}}(j\omega, \vec{r})$, whose discretized (computed) values at discrete frequencies ω_n are described through Roman upright fonts as $\breve{\mathbf{C}}(j\omega_n)$. Corresponding macromodels are denoted as $\mathbf{C}(s)$ in the Laplace-domain and $\mathbf{c}(t)$ in the time domain, with the accent $\breve{}$ removed.

III. Passive Macromodeling and Recursive Convolution

Any conversion from frequency-domain (tabulated responses) to a time-domain form is here performed through well-established *macromodeling* techniques. The latter are essentially based on the construction of a suitable rational approximation in the Laplace domain from the available samples, followed by either a state-space realization and equivalent circuit (in SPICE form) synthesis, or by an analytic Laplace transform inversion, which produces a closed-form expression of the impulse response at hand. We use macromodeling here since the developments over the last two decades have led to a set of mature, reliable, robust and efficient algorithms (see, e.g., [29]), now routinely used for research and production both in academia and in industry.

A. Passive macromodels of multiport systems

The lumped circuit simulation problem depicted in Fig. 1e is here performed using a standard SPICE solver. Therefore, an equivalent circuit for the multiport impedance matrix of the stucture is needed. Starting from the tabulated multiport impedance samples $\breve{\mathbf{Z}}(j\omega_n)$ obtained from the field solver, we apply a standard Vector Fitting (VF) process [29], [30] in its fast and decoupled implementation [31]. The number of poles is automatically determined through the so-called "Adding and Skimming process" described in [32]. The resulting rational

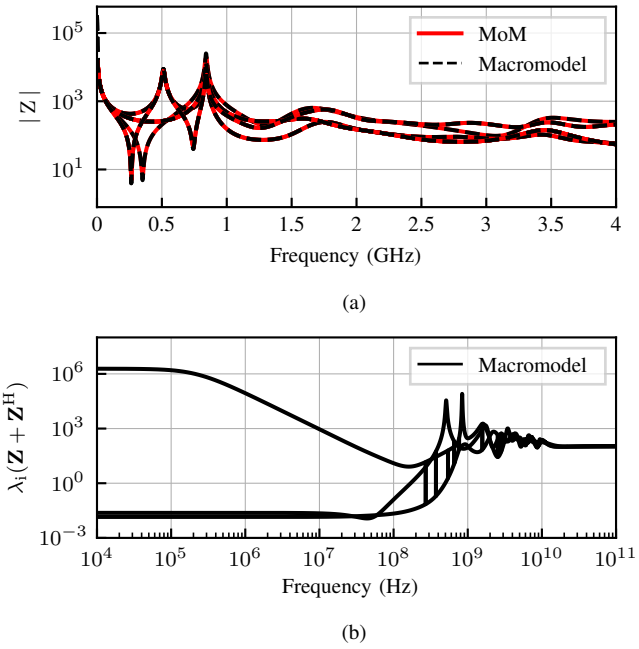

Fig. 2. (a): Impedance parameters of structure shown in Fig. 6 computed using MoM and corresponding extracted passive macromodel. (b): model passivity is confirmed by nonnegative frequency-dependent eigenvalues of the Hermitian part of $\mathbf{Z}(j\omega)$.

approximation is subjected to a passivity enforcement based on [33] (see also [29] for full details), yielding the positive real rational function

$$\mathbf{Z}(s) = \sum_{l=1}^{L} \frac{\boldsymbol{R}_l}{s - p_l} + \boldsymbol{R}_0 + s\boldsymbol{R}_{-1}. \tag{1}$$

where s is the complex frequency (Laplace variable), p_l are the poles of the model, here assumed to be common to all transfer function entries in order to model correctly global resonances, $\boldsymbol{R}_l$ are the residues corresponding to the poles p_l and $\boldsymbol{R}_0, \boldsymbol{R}_{-1}$ capture direct coupling and an inductive (linear) term. Using standard methods [29] the model (1) is realized as a state-space form and converted to a SPICE netlist. Figure 2 demonstrates model accuracy (top panel) and passivity (bottom panel) for a three-port two-loop antenna, introduced later in Sec. V-A, see Fig. 6.

B. Delay-rational fitting and fast recursive convolution

As discussed in Sec. II, all field coupling and radiation operators are naturally described in the frequency domain. However, accounting for nonlinear elements according to our proposed hybrid approach requires coupling and radiation to be formulated in time-domain. Therefore, we follow the same idea of closed-form Laplace inversion based on a suitable set of macromodels obtained from tabulated data from the MoM solver. There are however two main differences with respect to the impedance macromodel discussed in Sec. III-A;

- Since distances between structure and observation points may be significant in terms of wavelength at the highest frequency of interest, it is appropriate to embed the propagation effects in form of a time-delay term in both the Laplace-domain and the corresponding time-domain forms.
- Since only a forward evaluation of such operators is required, there is actually no need to check and enforce passivity of the rational approximation, which is instead essential for the impedance matrix macromodel in order to guarantee stable transient simulations.

Based on these considerations, we consider for each individual (scalar) frequency-domain operator $\breve{\mathcal{H}}(j\omega)$ a delay-rational approximation in form

$$H(s) = e^{-s\tau} \cdot \left(\sum_{l=1}^{\bar{l}} \frac{r_l}{s - p_l} + r_0 \right) \tag{2}$$

which is constructed by enforcing a fitting condition $H(j\omega_n) \approx \breve{\mathrm{H}}(j\omega_n)$ at all available samples from the MoM solver using the Delay Vector Fitting (DVF) algorithm [31], with a simplified implementation since only one delay term τ is required.

Assuming that operator $\breve{\mathcal{H}}(j\omega)$ is applied to some input signal $U(j\omega)$ to obtain some output $Y(j\omega)$, the corresponding time-domain form based on approximation (2) reads

$$\begin{aligned} y(t) &= \mathrm{h}(t) * u(t) \\ &= \sum_{l=1}^{\bar{l}} e^{p_l t}\theta(t) * u(t-\tau) + r_0 u(t-\tau) \end{aligned} \tag{3}$$

where θ is the Heaviside step function. Thanks to the exponential kernels, the evaluation of the output $y(t)$ at any time instant t can be performed through an interpolation of discrete output samples obtained through recursive convolutions. Defining a delayless output $z(t)$ such that $y(t) = z(t-\tau)$, and discretizing the time axis with resolution T, the discrete samples $z_k = z(t_k)$ at uniformly sampled time steps $t_k = kT$ are simply obtained as

$$z_k = \sum_{l=1}^{\bar{l}} r_l x_{l,k} + r_0 u_k \tag{4}$$

with

$$x_{l,k} = \alpha_l x_{l,k-1} + \beta_l u_k + \gamma_l u_{k-1} \tag{5}$$

through constant and pre-computed coefficients $\alpha_l, \beta_l, \gamma_l$ (see [29] for detailed expressions). Then, defining $\Delta = \tau/T - K$ and $K = \lfloor \tau/T \rfloor$, with operator $\lfloor \cdot \rfloor$ denoting truncation to the largest integer not larger than its argument, we have

$$y(t) = z(t-\tau) \approx (1-\Delta) z_{k-K} + \Delta z_{k-K-1} \tag{6}$$

Throughout the following, we will denote the above discretized delayed recursive convolution with the compact notation

$$y(t) = \mathrm{h}(t) \circledast u(t) \tag{7}$$

We remark that numerical evaluation of (7) is particularly efficient since both CPU and memory costs scale linearly with number of time steps to be computed.

IV. Numerical Implementation

A. Characterization of Field Coupling at Lumped Ports

The objective of this section is to describe the computation of the voltage sources $\boldsymbol{V}_{\text{oc}}(j\omega)$ and the impedance parameters $\breve{\mathbf{Z}}(j\omega)$ to construct the Thevenin equivalent as shown in Fig. 1d. To this end, we remove the lumped nonlinear loads and we solve the resulting linear field coupling problem in the frequency domain using MoM. A qualitative description of a numerically efficient implementation of the above steps is as follows; all patches of the PEC structure experience an impressed tangential electric field, which is canceled by the field of the induced currents (to be computed) on the structure s.t. the electric field tangential to the structure except at the ports is zero. This requires the computation of the mutual coupling of the patches which is stored in an impedance matrices for each frequency point, which can be written

$$\begin{bmatrix} \breve{\mathbf{Z}}_{11} & \breve{\mathbf{Z}}_{12} \\ \breve{\mathbf{Z}}_{21} & \breve{\mathbf{Z}}_{22} \end{bmatrix} \cdot \begin{bmatrix} \vec{I}_s^{\,i} \\ \vec{I}_p^{\,i} \end{bmatrix} = \begin{bmatrix} \vec{V}_s^{\,i} \\ \vec{V}_p^{\,i} \end{bmatrix}, \tag{8}$$

where $\vec{I}_s^{\,i}$ are the unknown currents across the patches, $\vec{I}_s^{\,i}$ are the short circuit port currents $\vec{V}_s^{\,i}$ and $\vec{V}_p^{\,i}$ are the voltages compensating the incident field tangential to the patches and ports, respectively. Frequency sampling rate (N samples at frequencies ω_n) and bandwidth are determined based on the bandwidth of the excitation pulse as well as on the expected resonance pattern, so that each resonance is well resolved.

Network parameters: The first step is to determine the network parameters of the structure at the lumped ports. The reduced admittance matrix $\breve{\mathbf{Y}}(j\omega_n)$ is calculated from (8) by solving for the image of each port excitation (1 V at the ports, all other voltages 0 V) separately and selecting only the rows corresponding to port currents from the resulting solution matrix. These results are then collected into the $\mathrm{P}\times\mathrm{P}$ port admittance matrix $\breve{\mathbf{Y}}(j\omega_n)$, which is then inverted at each frequency to obtain the open-circuit impedance matrix $\breve{\mathbf{Z}}(j\omega_n)$. The computational cost is $\mathcal{O}(\mathrm{N}_u^3)$, where N_u is the number of unknowns. The memory requirement of patch coupling matrix is $\mathcal{O}(\mathrm{N}_u^2)$ and grows linearly with the number of frequency points. A detailed numerical complexity analysis conducted in [34]. Alternatively, the admittance matrix can be computed in one single step (For each frequency point) by computing a Schur complement to (8) for eliminating internal patch variables. Our current implementation is based on the first approach. Even for large port numbers, this step has a computational cost that is significantly smaller than the total cost for the overall modeling flow.

These frequency samples are fed to the Vector Fitting algorithm followed by a passivity enforcement postprocessing, as discussed in Sec. III-A, leading to a state-space macromodel. The latter is synthesized as a SPICE equivalent circuit [29].

Computation of open-circuit voltages: We now consider the open-circuit voltages (Fig. 1b). For the sake of generality, we consider an incident field pattern composed by K independent plane waves characterized by their incidence/polarization angles $\{(\theta,\phi,\psi)^k\}$ and electric field spectra $E_{\text{inc}}^k(j\omega)$ for $k=1,\ldots,\mathrm{K}$. The relationship between each incident field waveform spectrum $E_{\text{inc}}^k(j\omega)$ and the corresponding induced open circuit voltage $V_{\text{oc}}^{k,p}(j\omega)$ at port p (see Fig. 1b) can be characterized by a transfer function $\breve{\mathcal{B}}^{k,p}(j\omega)$ and can be written as

$$V_{\text{oc}}^{k,p}(j\omega) = \breve{\mathcal{B}}^{k,p}(j\omega)\cdot E_{\text{inc}}^k(j\omega). \tag{9}$$

Computation of (9) is again achieved through application of a MoM solver [27], which uses the electric field integral equation (EFIE) in a mixed potential formulation. The matrix equation is solved by LU decomposition [35]. Stability issues have not been observed in previous comparable works [1], [2]. Investigations have shown that the resulting current distributions stay stable providing expected system responses even in case of internal resonances. The adopted solver returns tabulated frequency responses at discrete frequencies ω_n. These can be collected into a three-way tensor $\breve{\mathbf{B}}\in\mathbb{C}^{\mathrm{N}\times\mathrm{K}\times\mathrm{P}}$, by iterative and/or parallel execution of the MoM solver which solves the EFIE for each set of tuples $\{(\theta,\phi,\psi)^k\}$ defining plane wave excitations of unit amplitude over N frequency samples ω_n. As a result, the open-circuit voltages are expressed at each frequency ω_n as

$$V_{\text{oc}}^{p}(j\omega_n) = \sum_{k=1}^{\mathrm{K}} \breve{\mathrm{B}}^{k,p}(j\omega_n) E_{\text{inc}}^k(j\omega_n). \tag{10}$$

Rational fitting is then used as a postprocessing to convert the equivalent to time-domain form that is immediately usable for transient analysis.

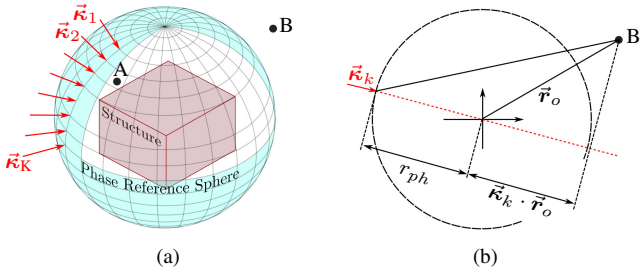

Fig. 3. (a): visualization of phase reference sphere with radius r_{ph}. (b): consequently to the reference shift, the distance traveled by a plane wave to reach observer B changes due to the new reference plane. See text for details.

Setting of phase reference planes: As in most common implementations, the adopted MoM solver [27] sets the reference phase of an incident plane wave field at the origin of the coordinate system. Therefore, depending on the location of the lumped ports with respect to the plane wave propagation direction, the impulse response $\mathrm{b}^{k,p}(t)$ associated to the transfer functions $\breve{\mathcal{B}}^{k,p}(j\omega)$ may not satisfy the fundamental causality conditions $\mathrm{b}^{k,p}(t) = 0$ for $t<0$. The latter is however essential for later time-domain lumped circuit solution with nonlinear elements connected, due to the time-stepping nature of all transient analysis methods available in any circuit solver. For the transient scattering problem to be well-defined, we will require all incident fields to vanish identically in a volume that encloses the PEC structure under investigation for all times $t<0$. For this reason, we define the reference phase of incident plane waves on the surface of a sphere of

radius r_{ph} centered at the origin of the coordinate system, which completely includes the structure under investigation, see Fig. 3a. Correspondingly, we introduce the phase-shifted transfer functions

$$\bar{\mathrm{B}}^{k,p}(j\omega_n) = e^{-j\omega_n \frac{r_{ph}}{c_0}} \cdot \breve{\mathrm{B}}^{k,p}(j\omega_n) \tag{11}$$

where c_0 is the speed of light in free space. The term $\frac{r_{ph}}{c_0}$ corresponds to the propagation delay of the plane wave from the reference sphere to the origin, which is now embedded as a delay term in the transfer functions $\bar{\mathrm{B}}^{k,p}(j\omega_n)$.

We are now ready to perform a time-domain conversion of (9). Instead of using a standard FFT processing, we choose the more flexible approach of Sec. III-B of performing a delay-rational approximation of each phase-shifted transfer function $\bar{\mathrm{B}}^{k,p}(j\omega_n)$, followed by a recursive convolution. The result is

$$v_{\mathrm{oc}}^{p}(t) = \sum_{k=1}^{\mathrm{K}} \bar{\mathrm{b}}^{k,p}(t) \circledast \mathcal{E}_{\mathrm{inc}}^{k}(t), \tag{12}$$

where by consruction $\bar{\mathrm{b}}^{k,p}(t) = 0$ for $t < 0$. We remark that this implementation choice allows, for instance, for persistently exciting and non-periodic field waveforms and provides a simpler approach for handling bandlimited data without introducing aliasing effects.

B. Solution of Transient Port Voltages with nonlinear Loading

We now address the lumped circuit problem of Fig. 1e, whose individual components are fully characterized based on the results of Sec. IV-A. In particular, the impedance matrix is available as a macromodel in SPICE-compatible form, whereas the time-domain open-circuit voltages are available through the recursive convolutions of (12) and are synthesized as piecewise linear sources for SPICE transient analysis.

The nonlinear loads are assumed to have general voltage-current characteristics, compactly collected as $\boldsymbol{v} = \mathcal{F}(\boldsymbol{i})$. These are reattached to the ports of the Thevenin equivalent, and the resulting circuit is solved using an off-the-shelf circuit solver [37]. We denote the corresponding differential-algebraic equation formulation embedded in such a solver by the abstract notation

$$\boldsymbol{v} = \mathcal{N}(\mathcal{F}, \mathbf{Z}, \boldsymbol{v}_{\mathrm{oc}}) \tag{13}$$

where $\mathcal{N}$ represents the used nonlinear circuit solver, and where the desired output variables being computed are the transient port voltages $\boldsymbol{v}$. This solution is depicted with a blue box in Fig. 4.

C. Computation of Field at Observation Points

Once the port voltages $\boldsymbol{v}(t)$ induced on the nonlinearly loaded structure by the incident field are known, we can proceed in computing the (total) field at desired observation points $\vec{\boldsymbol{r}}_o$, with $o = 1, \ldots, O$. As described in Fig. 1g. This is accomplished by solving a linear scattering problem defined by replacing the nonlinear elements with equivalent (known) voltage sources $\boldsymbol{v}(t)$, available from the lumped circuit solution of Sec. IV-B.

As depicted in Fig. 1h, the total field at $\vec{\boldsymbol{r}}_o$ can be expressed as the superposition of three terms as

$$\begin{aligned}\vec{\boldsymbol{E}}_{\mathrm{obs}}(j\omega, \vec{\boldsymbol{r}}_o) = &\sum_{d=1}^{3}\sum_{p=1}^{\mathrm{P}} \breve{\mathcal{C}}^{o,p,d}(j\omega) V^{p}(j\omega) \cdot \vec{\boldsymbol{e}}_d \\ &+ \sum_{d=1}^{3}\sum_{k=1}^{\mathrm{K}} \breve{\mathcal{D}}^{o,k,d}(j\omega) E_{\mathrm{inc}}^{k}(j\omega) \cdot \vec{\boldsymbol{e}}_d, \\ &+ \vec{\boldsymbol{E}}_{\mathrm{inc}}(j\omega, \vec{\boldsymbol{r}}_o),\end{aligned} \tag{14}$$

where $\vec{\boldsymbol{e}}_d$ for $d = 1, 2, 3$ denotes the unit vector in the x, y or z direction, $\breve{\mathcal{C}}^{o,p,d}$ is the operator mapping the *voltage* at port p to the d-th component of the scattered electric field at the observer o with all other ports shorted, and $\breve{\mathcal{D}}^{o,k,d}$ is the operator mapping the k-th *incident plane wave* to the d-th component of the scattered electric field at the observer o, with all ports shorted. The contribution from the incident field to the total field is known and does not require any further processing.

All operators $\breve{\mathcal{C}}^{o,p,d}$ and $\breve{\mathcal{D}}^{o,k,d}$ are computed using MoM and are available as tabulated frequency data, collected respectively in tensors $\breve{\mathbf{C}}(j\omega_n) \in \mathbb{C}^{\mathrm{O}\times\mathrm{P}\times 3}$ and $\breve{\mathbf{D}}(j\omega_n) \in \mathbb{C}^{\mathrm{O}\times\mathrm{K}\times 3}$. We are now ready to cast (14) in time-domain. This is accomplished by the following three steps.

- A delay-rational approximation is computed for each component of $\breve{\mathbf{C}}(j\omega_n)$ using the procedure of Sec. III-B, resulting in a set of discretized time-domain impulse responses represented by delayed recursive convolution operators $\mathrm{c}^{o,p,d}$;
- The same procedure is applied to each component of $\breve{\mathbf{D}}(j\omega_n)$, for which however we need to apply the same phase shift preprocessing as in (11), in order to align the time axis and enforce causality of all involved transfer functions. The result is a set of delayed recursive convolution operators $\bar{\mathrm{d}}^{o,k,d}$;
- In order to guarantee consistency among all field components, also for the direct incident field contribution the same delay is extracted and embedded into a set of free-space propagation operators $\bar{\mathrm{p}}^{o,k,d}$.

The final time-domain formulation enabling fast evaluation of total field at $\vec{\boldsymbol{r}}_o$ reads

$$\begin{aligned}\vec{\boldsymbol{\mathcal{E}}}_{\mathrm{obs}}^{\,o}(t) = &\sum_{d=1}^{3}\sum_{p=1}^{\mathrm{P}} \mathrm{c}^{o,p,d}(t) \circledast v^{p}(t) \cdot \vec{\boldsymbol{e}}_d \\ &+ \sum_{d=1}^{3}\sum_{k=1}^{\mathrm{K}} \bar{\mathrm{d}}^{o,k,d}(t) \circledast \mathcal{E}_{\mathrm{inc}}^{k}(t) \cdot \vec{\boldsymbol{e}}_d \\ &+ \sum_{d=1}^{3}\sum_{k=1}^{\mathrm{K}} \bar{\mathrm{p}}^{o,k,d}(t) * \mathcal{E}_{\mathrm{inc}}^{k}(t) \cdot \vec{\boldsymbol{e}}_d\end{aligned} \tag{15}$$

The first two lines in (15) are numerically computed using fast recursive convolution as in (5)-(6), whereas the last line is a simple time shift by a propagation delay $\tau_{k,o}$ depending on the excitation direction and the location of observer (see Fig. 3b) as

$$\tau_{k,o} = \frac{1}{c_0}\left(r_{ph} + \vec{\boldsymbol{\kappa}}_k \cdot \vec{\boldsymbol{r}}_o\right), \tag{16}$$

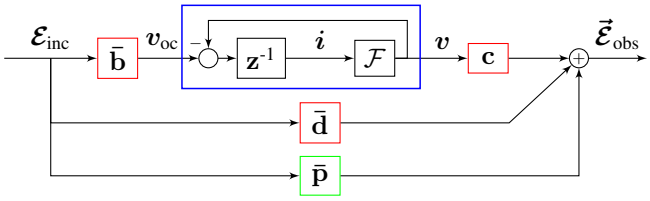

Fig. 4. Block diagram of operators used in time domain field computation. All red blocks correspond to time-domain operators implemented by discrete delayed recursive convolutions based on suitably computed delay-rational macromodels. The blue block is computed through a circuit solver, and the green block in the bottom is known in closed form. See text for details.

where c_0 is the speed of light in free space and $\vec{\boldsymbol{\kappa}}_k$ is the unit vector defining the propagation direction of the k-th excitation.

V. Numerical Experiments and Comparison to FIT Approach

The presented method is now illustrated and validated using various test cases. Since the main application we have in mind is energy selective shielding, we design all test cases to capture all features that are relevant for this application. In particular, each case will consist of three main components:

1) a PEC structure with well-defined (lumped) ports,
2) nonlinear port terminations,
3) excitations defined by incident field waveforms and directions of arrival.

The following subsections investigate different setups consisting of these components, by comparing the results of our proposed hybrid approach to reference time-domain solutions obtained through a commercial Finite Integration Technique (FIT) solver [38], which allows for direct transient simulations with embedded nonlinear terminations.

Due to the different modeling approaches of the adopted MoM solver and the FIT-based validation solver, certain differences in the final results are to be expected. We were able to identify two main reasons for such differences, namely the presence of an absorbing bounding box to truncate the computational domain in FIT (not required by proposed approach) and the lumped port implementation, which is different between the two solvers. These two points are addressed in Sec. V-A and Sec. V-B, respectively, together with a description of the compensation techniques that we adopt to make results directly comparable.

A. Effects of Computational Domain Truncation in FIT

In order to compute the electromagnetic properties of a structure using FIT (or any partial differential equation solver), it is necessary to limit the domain of computation. For free space problems, this is achieved by encapsulating the structure in a bounding box, which mimics an open domain by absorbing radiated fields with low reflection. The state of the art implementation involves using an absorbing PML.

Ideally, the bounding box should be large enough to include the reactive nearfield, whose extension can be estimated by $d = \frac{\lambda_{max}}{2\pi}$ [39], where λ_{max} is the largest (relevant) occurring wavelength in the simulation. Practically, a trade-off between computational cost and accuracy has to be made, leading to the usual practice of choosing the smallest possible box size that is compatible with accuracy requirements.

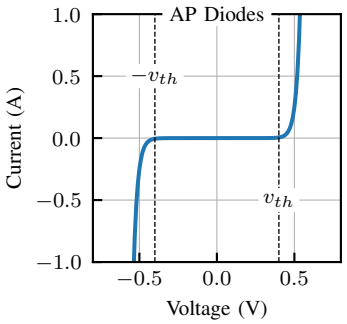

Fig. 5. V-I curve of two anti-parallel diodes (default model from [37] with saturation current $i_s = 1\,\text{nA}$). The threshold voltage is approximately $V_{th} = 0.4\,\text{V}$.

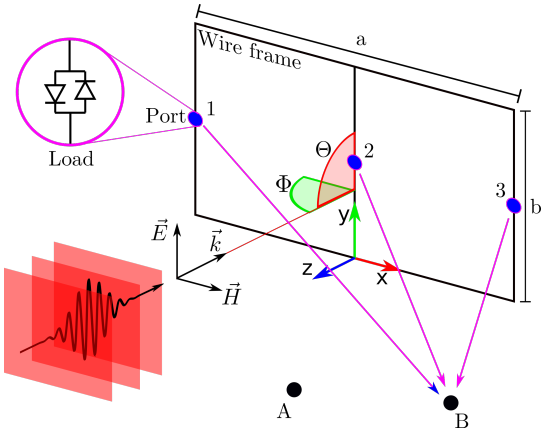

Fig. 6. A double-loop PEC frame with sizes $a = 15\,\text{cm}$ and $b = 10\,\text{cm}$. The frame is constructed from thin strips of width $5\,\text{mm}$. A plane wave pulse excites the structure from broadside, and the nonlinearly scattered field is observed at B. The three ports are loaded with the anti-parallel diode configuration displayed in Fig. 5. The diodes are aligned with the electric field vector of the incident pulse.

For our particular application, the nonlinear loads can cause mixing to lower frequencies and rectification (see later Fig. 10), which can dramatically increase the extension of the nearfield, thus requiring a larger PML bounding box. However, the PML size is usually determined a priori, since the frequency mixing properties of the loaded structure are difficult to predict a priori. Therefore, a careful assessment of the accuracy loss induced by a given PML size is mandatory for a correct interpretation of the validation results. The accuracy loss due to a finite-size computational domain in FIT is well described by a simple simulation setup, aimed at the evaluation of the driving point impedance matrix of the structure. For illustration, we consider the two-loop structure depicted in Fig. 6 with three lumped ports. The top panel of Fig. 7 compares the real part of the driving point impedance $\Re(Z_{11})$ obtained by FIT (distance from structure to PML from $25\,\text{mm}$ to $800\,\text{mm}$) and MoM, respectively. Since the structure is lossless (all metal is PEC), we expect the real part of the impedance to approach zero. This is indeed confirmed

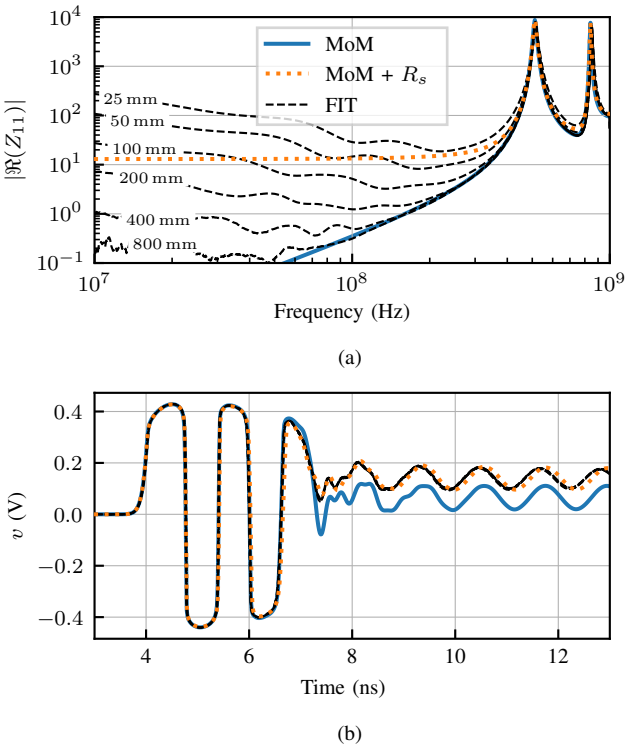

Fig. 7. (a): effect of FIT bounding box of different sizes on real part of the impedance for the two-loop structure of Fig. 6. For low frequencies, the nearfield of the structure extends into the PML, leading to absorption of energy and constituting a modeling error when trying to model a free space environment. (b): port voltage induced by an incident gaussian pulse (see text for definition) with all ports terminated into antiparallel diodes with threshold voltage $V_{th} = 0.4\,\mathrm{V}$. Adding a series resistance $R_s = 12\ \Omega$ to the MoM impedance confirms that the modeling error in FIT is due to artificial losses.

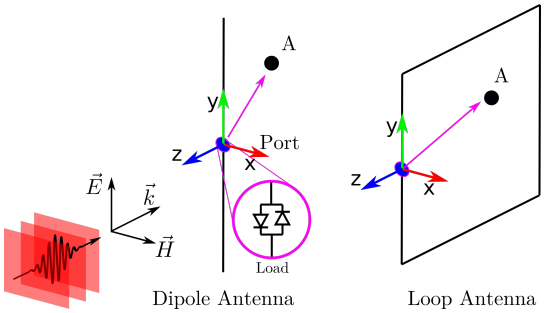

Fig. 8. Two canonical structures used for the validation of proposed approach. Left: electrical dipole of length 10 cm; right: square loop with area $100\,\mathrm{cm}^2$. A single port is defined for both structures as a feed gap of width $\Delta = 2\,\mathrm{mm}$. The diodes terminating the ports are aligned with the electric field vector of the incident pulse.

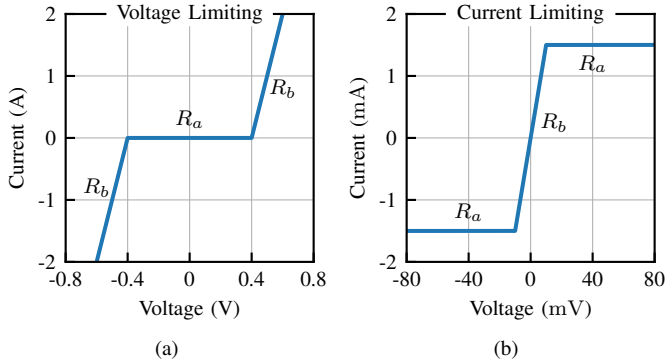

Fig. 9. Piecewise linear diode terminations ((a): voltage-limiting; (b): current-limiting). The differential resistance value of each branch is $R_a = 100\,\mathrm{k}\Omega$ and $R_b = 100\,\mathrm{m}\Omega$. The threshold voltage of the voltage limiting diode is $V_{\mathrm{th}} = 0.4\,\mathrm{V}$ and the threshold current of the current limiting diode is $I_{\mathrm{th}} = 1.5\,\mathrm{mA}$.

by the MoM results, whereas the FIT results lead to a real part which artificially increases at low frequencies. This behavior can be associated to spurious additional losses induced by the PML. A crude model for this spurious behavior can be obtained by adding a series resistance R_s to the impedance parameters computed by MoM, as confirmed in Fig. 7 (where a value $R_s = 12\ \Omega$ is considered). In order to confirm that these additional losses are due to the PML, we compare the low frequency behaviour of $\Re(Z_{11})$ of different bounding box sizes. The top panel of Fig. 7 shows that the frequency band over which the FIT impedance matches the MoM results extends more and more to lower frequencies as the PML size increases.

The effect of the spurious losses introduced by PML are also clearly visible in time-domain responses. The bottom panel of Fig. 7 compares the induced port voltage $v_1(t)$ by an incident plane wave gaussian pulse [40] on the same structure of Fig. 6 given by

$$\mathcal{E}_{\mathrm{inc}}(t) = \hat{E} \cdot e^{-a(t-\tau)^2} \cdot e^{j\omega_c(t-\tau)} \tag{17}$$

$$a = -\frac{(\frac{\omega_c}{2} b_w)^2}{4 \cdot \log(10^{\frac{b_{wr}}{20}})} \tag{18}$$

where τ is a time-delay as required by the assumed reference phase definition (11), $\hat{E} = 100\,\mathrm{V\,m^{-1}}$ is the amplitude of the pulse, $\omega_c = 2\pi \cdot 0.75\,\mathrm{GHz}$ is the center angular frequency, $b_w = 2$ is the fractional bandwidth and $b_{wr} = -6$ is the reference level at which fractional bandwidth is calculated (dB). Further, all three ports are loaded by two antiparallel diodes (default model from [37], $V_{th} = 0.4\,\mathrm{V}$). The macromodel of the network parameters has 28 poles.

We note a different late-time DC offset as computed by our proposed hybrid approach and by a direct transient FIT simulation. This DC offset is due to the charge separation occurring in the top and bottom halves of the two loops when all diodes are non-conducting. As above, the proposed approach can be modified to match FIT results by adding the series resistance R_s in the SPICE simulation that evaluates the port voltage (Sec. IV-B), as depicted by the orange curve in the bottom panel of Fig. 7.

The above discussion pinpoints the main reason for incorrect DC offsets in late-time transient results, which is understood as spurious losses at low frequency induced by PML in FIT validations. The correctness of the low-frequency asymptotic behavior of MoM impedance is confirmed based on theoretical considerations, giving strong confidence in the corresponding transient results, which are subject of this investigation.

In order to provide meaningful validations in the following sections, we will avoid considering pathological cases

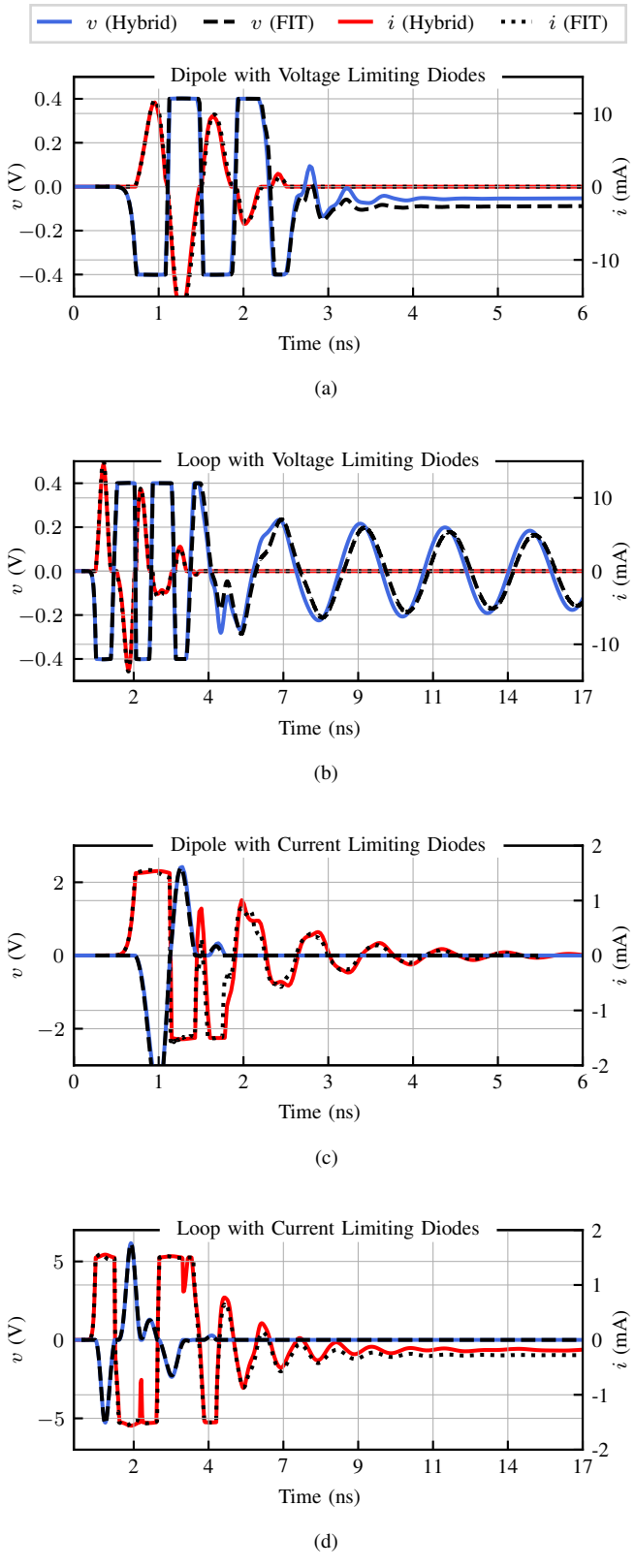

Fig. 10. Induced port voltage at the dipole and loop antenna shown in Fig. 8 when terminated with the anti-parallel, piecewise linear diode models shown in Fig. 9. The configurations are as follows: (a): dipole with voltage limiting diodes; (b): loop with voltage limiting diodes; (c): dipole with current limiting diodes; (d): loop with current limiting diodes. Configurations (a) and (d) allow for sustained DC components due to rectification in voltage and current, respectively. Therefore, discrepancies are expected. See text for details.

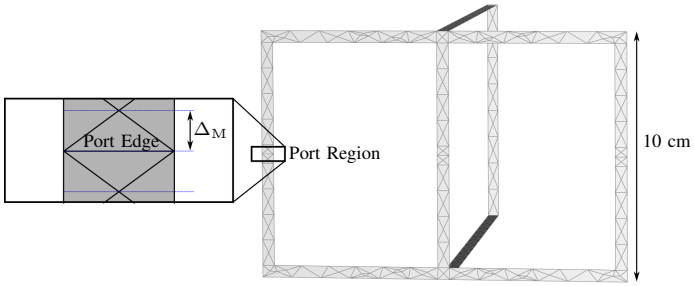

Fig. 11. Detailed view of the mesh in the port region of the structure presented in 13, highlighting the patch height $\Delta_M = 1.25\,\mathrm{mm}$.

for which the FIT approach is problematic due to domain truncation. These cases can be characterized as those structure-load combinations that sustain DC components at late time as an effect of rectification from nonlinear loads. Two canonical structures that can be used as templates are the dipole and the single loop depicted in Fig. 8 (network macromodels have 10 and 20 poles, respectively), together with voltage-limiting and current-limiting diode terminations, whose characteristics are depicted in Fig. 9. The dipole with voltage-limiting diodes and the loop with current-limiting diodes support a DC voltage and current, respectively, when excited by an incident gaussian pulse ($\hat{E} = 80\,\mathrm{V\,m^{-1}}$, $\omega_c = 2\pi \cdot 1.5\,\mathrm{GHz}$, $b_w = 2$, $b_{wr} = -6$, see eq. (17)). The corresponding late-time responses depicted in Fig. 10a and d, respectively, show indeed significant differences between our proposed approach and FIT. Conversely, the dipole with current-limiting diodes and the loop with voltage-limiting diodes do not support a late-time DC component, and correspondingly the FIT and the proposed approach match closely (Fig. 10b and c).

Throughout the following, we will only consider structures with voltage-limiting terminations having a conducting path even if the ports are open-circuited. In addition to being good templates for the energy-selective shielding applications, these loaded structures allow for accurate validation.

B. *Effects of Port Modeling in MoM*

The lumped port geometry and the corresponding different implementations available in the adopted field solvers provide another cause for potential differences in the computed results. Ideally, we would like to model each lumped port as defined by a pair of nodes on adjacent metal structures, located at a given finite distance Δ which is much smaller than the smallest wavelength of interest. This lumped port realization is directly available in the FIT solver that we use for validation. Conversely, the adopted MoM solver (as typical in both research and commercial codes) only supports delta-gap feeds [35], which implement infinitesimal gap ports (electric field only inside gap). Therefore, results from the two solvers in terms of both port voltages with or without terminations and network parameters are expected to disagree due to the different way in which the local fields surrounding the ports are represented.

Specifically, we found that the impedance parameters computed using the adopted MoM solver are sensitive to the

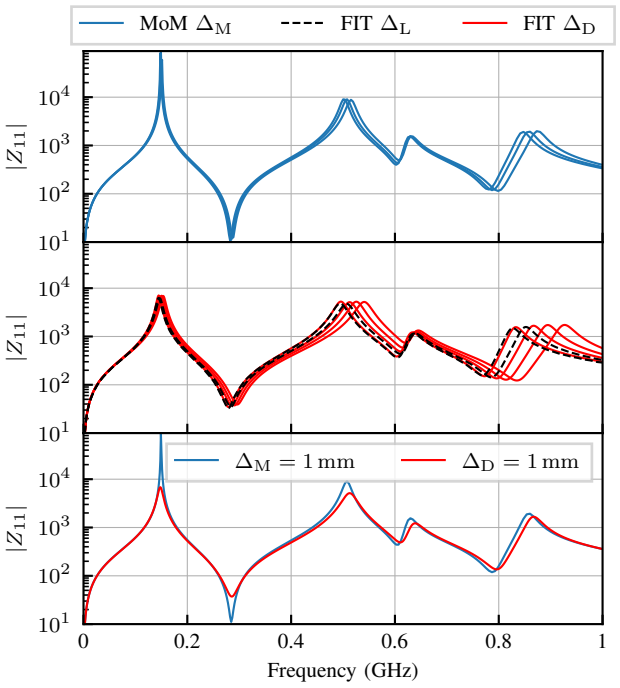

Fig. 12. Top panel: Z_{11} for the structure shown in Fig. 13 computed using the adopted MoM solver with different local port mesh settings (see Fig 11) with $\Delta_M \in \{0.5\,\mathrm{mm}, 2\,\mathrm{mm}, 4\,\mathrm{mm}\}$. Middle panel: Comparison of distributed and lumped port models available in the adopted FIT solver with port gaps Δ_D and Δ_L, respectively, in the range $0.5\,\mathrm{mm} - 4\,\mathrm{mm}$. Bottom panel: MoM and FIT results are in good agreement if $\Delta_M = \Delta_D = 1\,\mathrm{mm}$.

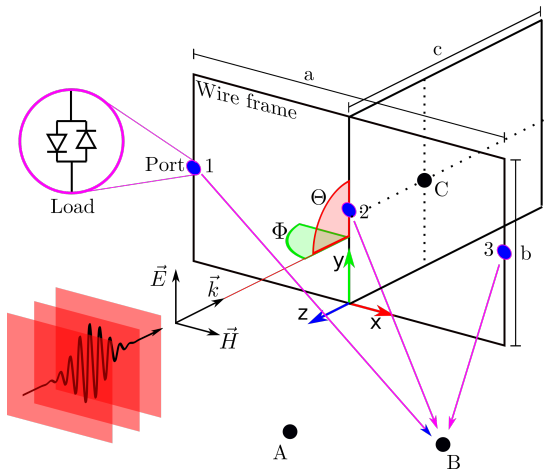

Fig. 13. A three-loop PEC frame, obtained from the structure of Fig. 6 by adding a third loop of size $c = 20\,\mathrm{cm}$ to ensure a conducting path even if the three ports are open-circuited. The port gap is set to $\Delta = 1.25\,\mathrm{mm}$.

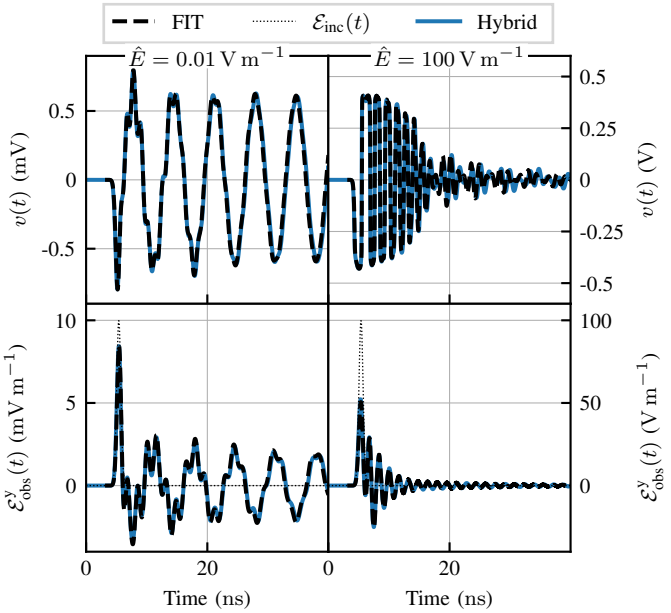

Fig. 14. Validation of port voltage and field at observer with FIT for the loop structure of Fig. 13 under weak (left) and strong (right) incident field. Top row: port voltages; Bottom row: total electric field at observation point C.

local meshing of the port region, depicted in Fig. 11. The top panel of Fig. 12 shows Z_{11} for the structure of Fig. 13 using $\Delta_M \in \{0.5\,\mathrm{mm}, 2\,\mathrm{mm}, 4\,\mathrm{mm}\}$. The sensitivity of the frequency response is moderate but clearly visible in the plots. The middle panel of Fig. 12 depicts the same network parameter Z_{11} obtained by FIT, using the two available port implementations in the adopted FIT solver: the "lumped" port model (dashed lines) and the "distributed" port model (solid lines) for different gap widths in the range $0.5\,\mathrm{mm} - 4\,\mathrm{mm}$. Changing the gap size induces variations in the frequency response as an effect of the variations in the local mesh, with however quite different behavior for the two port implementations. Both FIT models differ from the MoM model, as can be noted by comparing top and middle panel of Fig. 12. For this particular structure, there is a combination between port gap size and local mesh settings in MoM ($\Delta_M = \Delta_D = 1\,\mathrm{mm}$) for which both MoM and FIT results match accruately (bottom panel of Fig. 12). For this reason, all results in this paper will be computed by using these port settings in the MoM and FIT solvers, so that the influence of different port implementations is minimized in the validation results.

C. Coupled Loop Antenna

We now apply the presented method to the setup depicted in Fig. 13, which is chosen as a problem of small complexity. The ports are terminated with anti-parallel diodes (default model from [37] with a threshold voltage $V_{th} = 0.4\,\mathrm{V}$). The structure is illuminated by a low ($\hat{E} = 0.01\,\mathrm{V\,m^{-1}}$) and a high ($\hat{E} = 100\,\mathrm{V\,m^{-1}}$) amplitude gaussian pulse ($\omega_c = 2\pi \cdot 0.75\,\mathrm{GHz}$, $b_w = 2$, $b_{wr} = -6$). Comparing the induced voltages at port 1 for both excitation amplitudes (see top row of Fig. 14) clearly shows the nonlinear dependence of the system response on the excitation amplitude. Once the induced open circuit port voltage exceeds the threshold voltage of the diodes, voltage clipping occurs as displayed in the top right panel of Fig. 14.

The bottom row of Fig. 14 shows the computed electric field in y-direction for an observer located at point C with coordinates $(0, 5, -0.083)\,\mathrm{m}$, confirming nonlinear effects also on local fields. In fact, the maximum field strength for the weak excitation at the observer (left bottom panel) is roughly 80% of the excitation amplitude, which is significantly larger

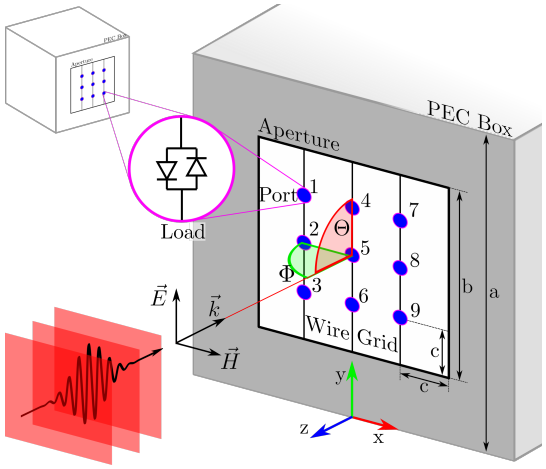

Fig. 15. Box with nonlinearly loaded grid across aperture introduced in [2]. All sides of the box are $a = 50\,\mathrm{cm}$, the square aperture is $b = 25\,\mathrm{cm}$ and the port spacing is $c = 6.25\,\mathrm{cm}$. The grid is modeled using patches with patch width $2\,\mathrm{mm}$. Nine ports loaded with antiparallel diodes connected to the grid create a field dependent shield. A gaussian modulated sinusoid with plane wave fronts excites the structure. The scattered field is measured at observers inside and outside of the cavity (observers not displayed).

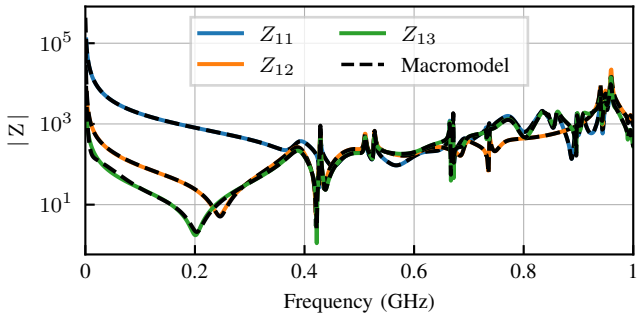

Fig. 16. The impedance parameters for the box with diode screen depicted in Fig. 15 computed using MoM and the extracted macromodel show good agreement.

compared to the strong excitation (right bottom panel), which is 50% of the excitation amplitude. In the remainder of this paper we will investigate structures that increase the effect of this energy selective shielding. In all cases, an excellent agreement is noted between proposed method and a reference FIT simulation.

D. Box with a Diode Screen across Aperture

In order to validate our approach also in case of a stronger energy selective shielding, we investigate the structure presented in [2] (shown in Fig. 15). The idea behind this design is the cover the aperture of a cavity with an energy selective diode grid, which is either transparent for small field strengths, and opaque for large field strengths. It can be understood as a more complex version of the coupled loops depicted in Fig. 13 with the difference that all energy entering the cavity must pass through the diode grid. This structure is computationally more expensive and exhibits sharper resonances due to the cavity. These are clearly visible in Fig. 16, which compares the impedance responses of the passive macromodel (44 poles

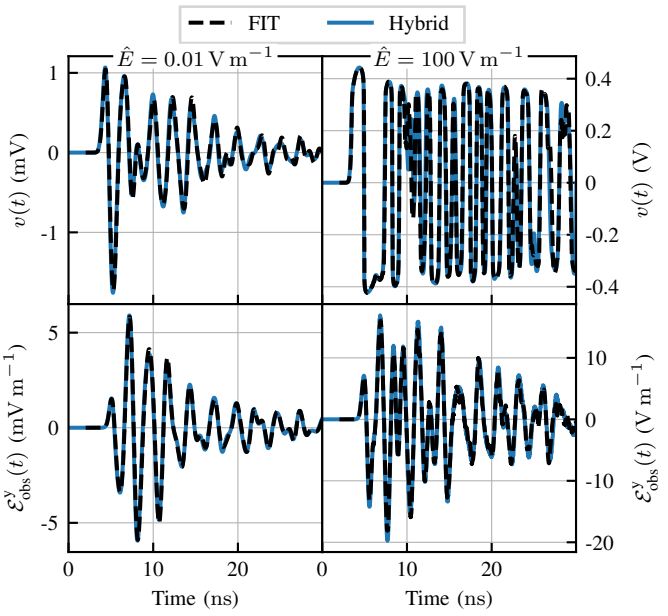

Fig. 17. Port voltage (top panels) and field at observer in y-direction (bottom panels) for the box with diode screen shown in Fig. 15. See text for details.

used) to the corresponding raw responses obtained by MoM. In the following, we compute the scattered fields using the presented method and compare against FIT with the following settings: all ports of the structure are terminated with antiparallel diodes (default model from [37], $V_{\mathrm{th}} = 0.4\,\mathrm{V}$), and the incident field waveform is a gaussian pulse ($\omega_c = 2\pi \cdot 0.75\,\mathrm{GHz}$, $b_w = 2$, $b_{wr} = -6$) with both low and high amplitude, $\hat{E} = 0.01\,\mathrm{V\,m^{-1}}$ and $\hat{E} = 100\,\mathrm{V\,m^{-1}}$, respectively. The resulting voltages at port 1 are shown in the top row of Fig. 17, demonstrating the nonlinear behaviour of the structure like in the previous subsection. The bottom row of Fig. 17 shows the magnitude of the electric field at an observer located inside the box, at coordinates $(6.25, 25, -6.25)\,\mathrm{cm}$. The strong nonlinear dependence of the field that penetrates the box on the excitation amplitude is again clearly visible. On one hand, the transient waveforms are different. On the other hand, although the ratio between strong and weak excitation amplitude is 10^4, the corresponding ratio computed on the peak-to-peak field amplitude at the observer is only 2×10^3. Equivalently, the maximum experienced field strength for the weak excitation at the observer (left bottom panel) is roughly 50% of the excitation amplitude, which is significantly larger compared to the strong excitation (right bottom panel), which is 20% of the excitation amplitude. Both proposed method and FIT provide almost identical results.

In order to quantify the shielding effectiveness of this structure, we define the shielding factor SF as the ratio of maximum observed field strength and the amplitude of the incoming pulse

$$\mathrm{SF} = \frac{\|\vec{\mathcal{E}}_{\mathrm{obs}}\|_\infty}{\|\mathcal{E}_{\mathrm{inc}}\|_\infty}, \tag{19}$$

where the shielding factor SF depends on the chosen observer, the pulse waveform, excitation direction and amplitude of the

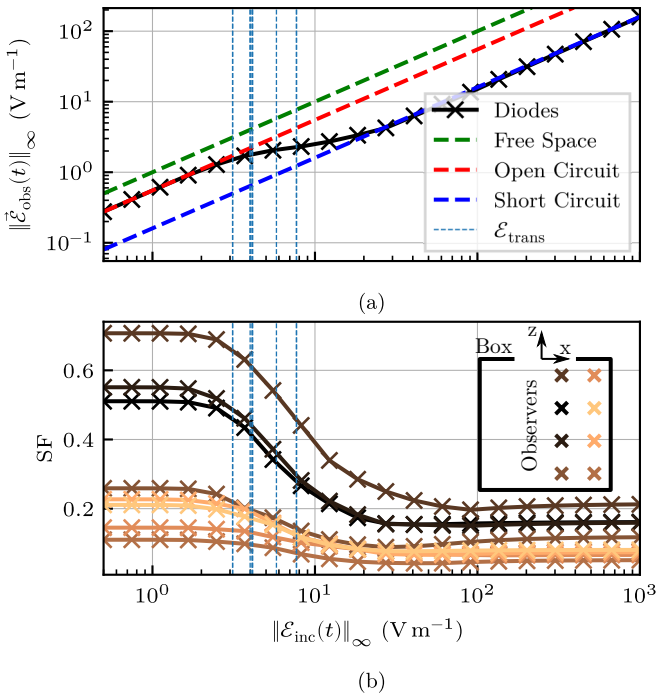

Fig. 18. (a): maximum electric field strength at a single observer inside the box depicted in Fig. 15 for different excitation amplitude. (b): shielding effectiveness of the same structure as a function of the incident field amplitude, for different observers inside the box where each line corresponds to a different location, as indicated by the markers in the pictograph in the top right. The pictograph shows the cross-section of the middle of the box with the aperture indicated by the gap in the square.

pulse. Figure 18 shows the shielding properties of the box with nine diodes (see Fig. 15) for different pulse amplitudes ($\omega_c = 2\pi \cdot 0.75\,\mathrm{GHz}$, $b_w = 2$, $b_{wr} = -6$). As expected, the transition from isolating to conducting of the diodes when increasing the excitation amplitude leads to an increase in SF. For both very small and very large field strengths, SF saturates. These limit cases can in fact be estimated using linear simulations with specific port terminations, namely open circuits to estimate the low-energy asymptote and short circuits to estimate the high-energy asymptote (see Fig. 18). We remark that the results for both these two limit conditions are available as part of the proposed modeling and simulation flow. Using the adopted notation, the open-circuit condition is achieved by setting $v = v_{\mathrm{oc}}$ in (15), yielding

$$\vec{\boldsymbol{\mathcal{E}}}_{\mathrm{obs}}(t) = \mathbf{c}(t) \circledast \boldsymbol{v}_{\mathrm{oc}}(t) + \bar{\mathbf{d}}(t) \circledast \boldsymbol{\mathcal{E}}_{\mathrm{inc}}(t) + \bar{\mathbf{p}}(t) * \boldsymbol{\mathcal{E}}_{\mathrm{inc}}(t). \tag{20}$$

Conversely, the short-circuit condition is achived by setting $v = 0$ in (15), leading to

$$\vec{\boldsymbol{\mathcal{E}}}_{\mathrm{obs}}(t) = \bar{\mathbf{d}}(t) \circledast \boldsymbol{\mathcal{E}}_{\mathrm{inc}}(t) + \bar{\mathbf{p}}(t) * \boldsymbol{\mathcal{E}}_{\mathrm{inc}}(t). \tag{21}$$

These equations yield approximations for the transient field hence the SF $v \ll V_{th}$ and $v \gg V_{th}$, providing the upper and the lower bound for SF, shown in Fig. 18.

The excitation amplitude $\mathcal{E}_{\mathrm{trans}}$ leading to the transition from isolating to conducting diodes can thus be estimated by setting $\|v_{\mathrm{oc}}\|_\infty = V_{th}$ in (12), which yields

$$\mathcal{E}_{\mathrm{trans}} = V_{th} \cdot \left[\frac{\|\mathrm{b}(t) \circledast \mathcal{E}_{\mathrm{inc}}(t)\|_\infty}{\|\mathcal{E}_{\mathrm{inc}}(t)\|_\infty} \right]^{-1}, \tag{22}$$

which are shown as vertical lines in Fig. 18 for all ports.

VI. Conclusion

The work presented here clearly shows that the computation of electrically large structures that are loaded with multiple nonlinear elements deserves renewed attention in the computational electromagnetics community. On one side there are novel applications like nonlinear shielding and nonlinear metasurfaces that will soon raise the bar above what has been typically handled by numerical computation so far. The optimization of structures that are several wavelengths large and contain hundreds of nonlinear elements are tasks that cannot be handled by any known method easily at this point. Hence, there is a need to develop fast and efficient methods. On the other side we have shown by careful comparison our own hybrid method with an established commercial solver that it is far from straightforward to achieve accurate and consistent results for this type of numerical problem. Hence, there is a need to further analyze and assess the pros and cons of each approach and to further develop alternative methods to move forward. We think that the hybrid method presented here offers a path to accurate and efficient computation of these types of problems especially in open spaces and in cases where an optimization of the nonlinear elements is required. Further studies will lead us in this direction.

Torben Wendt (S'17) received his B.S. and M.S. degree in electrical engineering from the Technical University Hamburg (TUHH), Hamburg, Germany, in 2014 and 2017, respectively.

Currently, he is working towards the Ph.D. degree at the Institute of Electromagnetic Theory, TUHH. He was a visiting researcher at the Politecnico di Torino for multiple times in 2018 and 2019. His current research interests include the modeling and simulation of nonlinear field circuit coupling in EMC applications.

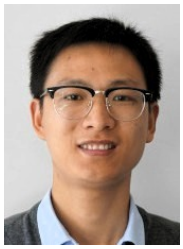

Cheng Yang (M'17) received his B.S. degree in electronic science and technology from Wuhan University (WHU), Wuhan, China, in 2009, the M.S. degree and the Ph.D. Degree with electromagnetic field and microwave technology from the National University of Defense Technology (NUDT), Changsha, China, in 2012 and 2016.

Since 2019 he has been a senior engineer of the Institute of Electromagnetic Theory, Technische Universität Hamburg (TUHH), Hamburg, Germany. From 2013 to 2015, he was funded by the Chinese Scholarship Council (CSC) as a joint-PhD student at TUHH. From 2016 to 2019, he was a Faculty Member of the State Key Laboratory of Millimeter Wave at Southeast University (SEU), Nanjing, China. His current research interests include computational electromagnetics, microwave measurement techniques, design and analysis of nonlinearly loaded electromagnetic structures.

Stefano Grivet-Talocia (M'98–SM'07–F'18) received the Laurea and Ph.D. degrees in electronic engineering from the Politecnico di Torino, Turin, Italy.

From 1994 to 1996, he was with the NASA/Goddard Space Flight Center, Greenbelt, MD, USA. He is currently a Full Professor of electrical engineering with the Politecnico di Torino. He co-founded the academic spinoff company IdemWorks in 2007, serving as the President until its acquisition by CST in 2016. He has authored over 150 journal and conference papers. His current research interests include passive macromodeling of lumped and distributed interconnect structures, model-order reduction, modeling and simulation of fields, circuits, and their interaction, wavelets, time-frequency transforms, and their applications.

Dr. Grivet-Talocia was a co-recipient of the 2007 Best Paper Award of the IEEE TRANSACTIONS ON ADVANCED PACKAGING. He received the IBM Shared University Research Award in 2007, 2008, and 2009. He was an Associate Editor of the IEEE TRANSACTIONS ON ELECTROMAGNETIC COMPATIBILITY from 1999 to 2001 and He is currently serving as Associate Editor for the IEEE TRANSACTIONS ON COMPONENTS, PACKAGING AND MANUFACTURING TECHNOLOGY. He was the General Chair of the 20th and 21st IEEE Workshops on Signal and Power Integrity (SPI2016 and SPI2017).

Christian Schuster (S'98 - M'00 - SM'05) received the Diploma degree in physics from the University of Konstanz, Germany, in 1996, and the Ph. D. degree in electrical engineering from the Swiss Federal Institute of Technology (ETH), Zurich, Switzerland, in 2000.

Since 2006 he is full professor and head of the Institute of Electromagnetic Theory at the Hamburg University of Technology (TUHH), Germany. Prior to that he was with the IBM T. J. Watson Research Center, Yorktown Heights, NY, where he was involved in high-speed optoelectronic package and backplane interconnect modeling and signal integrity design for new server generations. His currents interests include signal and power integrity of digital systems, multiport measurement and calibration techniques, and development of electromagnetic simulation methods for communication electronics.

Dr. Schuster received IEEE Transactions on EMC Best Paper Awards in 2001 and 2015, IEEE Transactions on CPMT Best Paper Awards in 2012 and 2016, IEC DesignCon Paper Awards in 2005, 2006, 2010, 2017 and 2018, three IBM Research Division Awards between 2003 and 2005, and IBM Faculty Awards in 2009 and 2010. Also, in 2019 he received the Sustained Service to the EMC Society Award. He is a member of the German Physical Society (DPG) and several technical program committees of international conferences on signal and power integrity, and electromagnetic compatibility. He was serving as a Distinguished Lecturer for the IEEE EMC Society in the period 2012-2013, as the Chair of the German IEEE EMC Chapter in the period 2016-2019 and is currently an Associate Editor for the IEEE Transactions on EMC and a member of the Board of Directors of the EMC Society.

REFERENCES

[1] A. Schröder, G. A. Rasek, H. Brüns, Z. Řezníček, J. Kučera, S. E. Loos, and C. Schuster, "Analysis of high intensity radiated field coupling into aircraft using the method of moments," *IEEE Trans. Electromagn. Compat.*, vol. 56, no. 1, pp. 113–122, Feb 2014.

[2] C. Yang, H.-D. Brüns, P. Liu, and C. Schuster, "Impulse response optimization of band-limited frequency data for hybrid field-circuit simulation of large-scale energy-selective diode grids," *IEEE Trans. Electromagn. Compat.*, vol. 58, no. 4, pp. 1072–1080, 2016. [Online]. Available: https://doi.org/10.1109/temc.2016.2540921

[3] S. Monni, D. J. Bekers, M. van Wanum, R. van Dijk, A. Neto, G. Gerini, and F. E. van Vliet, "Limiting frequency selective surfaces," in *2009 European Microwave Conference (EuMC)*, Sept 2009, pp. 606–609.

[4] ——, "Protection of RF electronics using tuneable frequency selective surfaces," in *2009 3rd European Conference on Antennas and Propagation*, March 2009, pp. 3170–3174.

[5] C. Yang, P.-G. Liu, and X.-J. Huang, "A novel method of energy selective surface for adaptive hpm/emp protection," *IEEE Antennas Wireless Propag. Lett.*, vol. 12, pp. 112–115, 2013. [Online]. Available: https://doi.org/10.1109/lawp.2013.2243105

[6] H. Wakatsuchi, D. Anzai, J. J. Rushton, F. Gao, S. Kim, and D. F. Sievenpiper, "Waveform selectivity at the same frequency," *Scientific Reports*, vol. 5, no. 1, p. 9639, 2015. [Online]. Available: https://doi.org/10.1038/srep09639

[7] G. V. Eleftheriades, "Protecting the weak from the strong," *Nature*, vol. 505, no. 7484, pp. 490–491, 2014. [Online]. Available: https://doi.org/10.1038/nature12852

[8] Z. Luo, X. Chen, J. Long, R. Quarfoth, and D. Sievenpiper, "Self-focusing of electromagnetic surface waves on a nonlinear impedance surface," *Applied Physics Letters*, vol. 106, no. 21, p. 211102, 2015. [Online]. Available: https://doi.org/10.1063/1.4921913

[9] ——, "Nonlinear power-dependent impedance surface," *IEEE Trans. Antennas Propag.*, vol. 63, no. 4, pp. 1736–1745, 2015. [Online]. Available: https://doi.org/10.1109/tap.2015.2399513

[10] S. Kim, H. Wakatsuchi, J. J. Rushton, and D. F. Sievenpiper, "Switchable nonlinear metasurfaces for absorbing high power surface waves," *Applied Physics Letters*, vol. 108, no. 4, p. 041903, 2016. [Online]. Available: https://doi.org/10.1063/1.4940712

[11] T. Sarkar and D. Weiner, "Scattering analysis of nonlinearly loaded antennas," *IEEE Trans. Antennas Propag.*, vol. 24, no. 2, pp. 125–131, 1976. [Online]. Available: https://doi.org/10.1109/tap.1976.1141327

[12] T. Sarkar, D. Weiner, and R. Harrington, "Analysis of nonlinearly loaded multiport antenna structures over an imperfect ground plane using the volterra-series method," *IEEE Trans. Electromagn. Compat.*, vol. EMC-20, no. 2, pp. 278–287, 1978. [Online]. Available: https://doi.org/10.1109/temc.1978.303720

[13] H. Xie, J. Wang, R. Fan, and Y. Liu, "A hybrid FDTD-SPICE method for transmission lines excited by a nonuniform incident wave," *IEEE Trans. Electromagn. Compat.*, vol. 51, no. 3 PART 2, pp. 811–817, 2009.

[14] R. Wang and J. M. Jin, "Incorporation of multiport lumped networks into the hybrid time-domain finite-element analysis," *IEEE Trans. Microw. Theory Tech.*, vol. 57, no. 8, pp. 2030–2037, 2009.

[15] S. Safavi and J. Ekman, "A hybrid PEEC–SPICE method for time-domain simulation of mixed nonlinear circuits and electromagnetic problems," *IEEE Trans. Electromagn. Compat.*, vol. 56, no. 4, pp. 912–922, Aug. 2014.

[16] K. Aygun, B. Fischer, and J. Meng, "A fast hybrid field-circuit simulator for transient analysis of microwave circuits," *IEEE Trans. Microw. Theory Tech.*, vol. 52, no. 2, pp. 573–583, 2004.

[17] F. Tesche and T. Liu, "Transient response of antennas with nonlinear loads," *Electronics Letters*, vol. 11, no. 1, p. 18, 1975. [Online]. Available: https://doi.org/10.1049/el:19750014

[18] T. Liu, F. Tesche, and F. Deadrick, "Transient excitation of an antenna with a nonlinear load: Numerical and experimental results," *IEEE Trans. Antennas Propag.*, vol. 25, no. 4, pp. 539–542, 1977. [Online]. Available: https://doi.org/10.1109/tap.1977.1141630

[19] A. Djordjevic and T. Sarkar, "Transient analysis of electromagnetic systems with multiple lumped nonlinear loads," *IEEE Trans. Antennas Propag.*, vol. 33, no. 5, pp. 533–539, 1985. [Online]. Available: https://doi.org/10.1109/tap.1985.1143611

[20] K. Deiseroth and H. Singer, "Transient analysis of nonlinearly loaded arrangements consisting of thin wires and metallic patches," *Proceedings of International Symposium on Electromagnetic Compatibility*, pp. 636–641, 1995. [Online]. Available: https://doi.org/10.1109/isemc.1995.523635

[21] D. Liao, "A hybrid approach for characterizing linear and nonlinear electromagnetic scattering : Theory and applications," No. ARL-TR-6261. ARMY RESEARCH LAB, Tech. Rep. November, 2012.

[22] K. Lee, "Analysis of large nonlinearly loaded antenna arrays under multitone excitation," *Microw. Opt. Technol. Lett.*, vol. 25, no. 5, pp. 319–323, Jun. 2000.

[23] V. Subramanian and A. E. Yilmaz, "An envelope-tracking hybrid field-circuit simulator for narrowband analysis of nonlinearly loaded wire antennas," *IEEE Trans. Microw. Theory Tech.*, vol. 62, no. 2, pp. 208–223, Feb. 2014.

[24] C. Yang, H.-D. Brüns, P. Liu, and C. Schuster, "Validation of a flexible causality treatment for transient analysis of nonlinearly loaded structures," in *2015 IEEE International Symposium on Electromagnetic Compatibility (EMC)*, 8 2015. [Online]. Available: https://doi.org/10.1109/isemc.2015.7256210

[25] A. Taflove, S. C. Hagness, and M. Piket-May, *Computational Electromagnetics: The Finite-Difference Time-Domain Method*, ser. The Electrical Engineering Handbook. Elsevier, 2005, pp. 629–670. [Online]. Available: https://doi.org/10.1016/b978-012170960-0/50046-3

[26] S. Silver, *Microwave antenna theory and design*. London, UK: P. Peregrinus on behalf of the Institution of Electrical Engineers, 1984, pp. 47–48.

[27] "Official website of CONCEPT-II," http://www.tet.tuhh.de/concept/, 2019.

[28] S. Maas, *Nonlinear microwave and RF circuits*. Boston, MA: Artech House, 2003, pp. 33–34.

[29] S. Grivet-Talocia and B. Gustavsen, *Passive Macromodeling*. John Wiley & Sons, Inc, 2015. [Online]. Available: https://doi.org/10.1002/9781119140931

[30] B. Gustavsen and A. Semlyen, "Rational approximation of frequency domain responses by vector fitting," *IEEE Trans. Power Del.*, vol. 14, no. 3, pp. 1052–1061, 1999. [Online]. Available: https://doi.org/10.1109/61.772353

[31] D. Deschrijver, M. Mrozowski, T. Dhaene, and D. D. Zutter, "Macromodeling of multiport systems using a fast implementation of the vector fitting method," *IEEE Microw. Wireless Compon. Lett.*, vol. 18, no. 6, pp. 383–385, 2008. [Online]. Available: https://doi.org/10.1109/lmwc.2008.922585

[32] S. Grivet-Talocia and M. Bandinu, "Improving the convergence of vector fitting for equivalent circuit extraction from noisy frequency responses," *IEEE Trans. Electromagn. Compat.*, vol. 48, no. 1, pp. 104–120, 2006. [Online]. Available: https://doi.org/10.1109/temc.2006.870814

[33] B. Gustavsen and A. Semlyen, "Enforcing passivity for admittance matrices approximated by rational functions," *IEEE Transactions on Power Systems*, vol. 16, no. 1, pp. 97–104, 2001. [Online]. Available: https://doi.org/10.1109/59.910786

[34] T. Wendt, C. Yang, S. Grivet-Talocia, and C. Schuster, "Numerical complexity study of solving hybrid multiport field-circuit problems for diode grids," September 2019, international Conference on Electromagnetics in Advanced Applications (ICEAA 2019).

[35] W. C. Gibson, *Method of moments in electromagnetics, second edition.* Apple Academic Press Inc, 2014. [Online]. Available: http://www.worldcat.org/oclc/870516721?referer=xid

[36] A. Vogt, H.-D. Brüns, Q. Wu, F. Gronwald, and C. Schuster, "A measurement setup for quantification of electromagnetic interference in metallic casings," *IEEE Trans. Electromagn. Compat.*, vol. 57, no. 6, pp. 1354–1364, 2015. [Online]. Available: https://doi.org/10.1109/temc.2015.2452295

[37] S. N. Laboratories, "Xyce analog circuit simulator," https://xyce.sandia.gov, 2019.

[38] Dassault Systems, "Microwave Studio," https://www.cst.com, 2019.

[39] C. Balanis, *Antenna theory : analysis and design*. Hoboken, New Jersey: John Wiley, 2016.

[40] "Scipy documention for gausspulse," https://docs.scipy.org/doc/scipy/reference/generated/scipy.signal.gausspulse.html, 2019.